Case Studies in Thermal Engineering 77 (2026) 107493

Contents lists available at ScienceDirect

Case Studies in Thermal Engineering

journal homepage: www.elsevier.com/locate/csite

The experimental and numerical study of battery thermal runaway influence on liquid cooling agent in the engineered fluid immersion system

Biao Zhou [a,*], Wei Li [a], Hideki Yoshioka [b], Kai Wang [a], Xukun Sun [b], Wei Wang [d], Tao Chen [c], Yike Guo [e], Zhenxiang Tao [a], Chenyang Jiang [a]

[a] *Inner Mongolia Research Institute, China University of Mining and Technology (Beijing), Ordos 017010, China*
[b] *Department of Architecture, Faculty of Engineering, the University of Tokyo, Tokyo 113-8654, Japan*
[c] *Tianjin Fire Science Technology Research Institute of MEM, Tianjin, 300381, China*
[d] *Shanghai Fire Science Technology Research Institute of MEM, Shanghai 200032, China*
[e] *Key Laboratory of Electrochemical Energy Safety Ministry of Emergency Management, Beijing 100012, China*

GRAPHICAL ABSTRACT

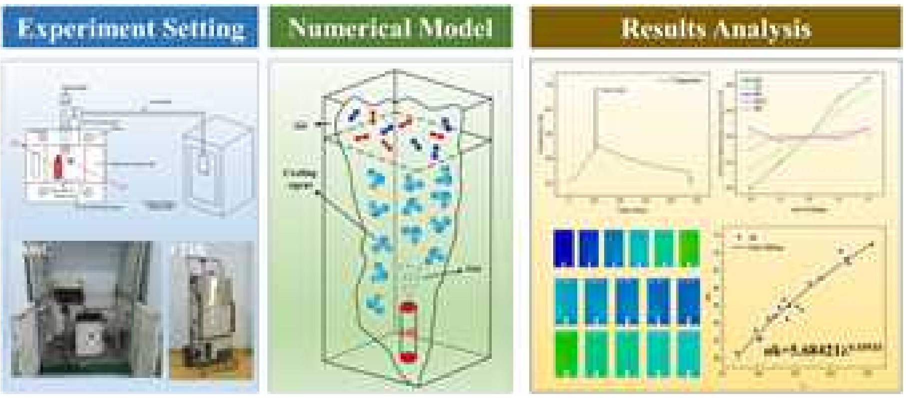

ARTICLE INFO

Keywords:
Cooling agent
Temperature rise rate
Lithium battery

ABSTRACT

This study aims to understand the temperature-increasing mechanism of the engineered fluid after high-temperature thermal runaway of a lithium-ion battery (LIB) under immersed liquid-cooled conditions. In this presentation, a series of experimental and numerical tests was

---

* Corresponding author.
E-mail address: zhoubiao1088@cumtb.edu.cn (B. Zhou).

https://doi.org/10.1016/j.csite.2025.107493
Received 14 November 2024; Received in revised form 30 October 2025; Accepted 30 November 2025

OpenFOAM
Thermal runaway

conducted to investigate the impact mechanism of thermal runaway on liquid cooling agents in an engineered fluid immersion system. The cylindrical 18650 thermal runaway's temperature profile is based on the Accelerating Rate Calorimeter (ARC) and Fourier Transform Infrared Spectrometer (FTIR). The numerical tests are conducted using the open-source software package OpenFOAM (version 7) by probing into the effects of its physical parameters on the rate of temperature rise concerning the HFE-7100 liquid. The relationship between parameters and the rate of temperature rise is clarified. Based on the results, a dimensionless consisting of the physical parameters such as boiling point, specific heat capacity, density, latent heat of vaporization, and Prandtl number of the liquid refrigerant on the temperature rise rate is quantitatively proposed. This provides a new method for developing next-generation refrigerants for LIB immersion in the future.

Nomenclature

α_i	Volume fraction
ρ_{vap}	Vapor phase density
ρ_{liq}	Liquid phase density
$\mathbf{u}$	Fluid vector velocity
Y	Fraction of phase components
f	Surface tension calculated by the stress model
$\dot{m}$	Evaporation rate per unit volume
E	Mixed energy
S_h	Source item
J_{lv}	mass transfer from the liquid phase to the vapor phase
J_{vl}	mass transfer from the vapor phase to the liquid phase
β	mass transfer time relaxation parameter
$T_{activate}$	Fluid boiling point
v	Turbulent viscosity
k	Kinetic energy
ε	Turbulent dissipation rate
P_k	Generation term of kinetic energy
C_v	Modelling coefficient for turbulent viscosity
D_k	Diffusion coefficient of turbulence
D_ε	Dissipation coefficient of turbulence
G	The generation rate of turbulent kinetic energy
S_k	Source item
$\mathbf{I}$	Unit tensor
D^*	Mesh scale
$\dot{Q}$	Total heat release rate
ρ_∞	Density
C_p	Specific heat
g	Gravitational constant
m	quality
m_0	Molar mass
T_0	Ambient temperature
ρ	Density
T	Boiling point
C_V	Constant pressure heat capacity
H	latent heat of vaporization
F	Surface tension
Pr	Prandtl number
ΔT	Temperature variation
h	Height
t	Thermal runaway time
$\mathbf{k}$	Temperature rising rate

1. Introduction

Lithium-ion batteries (LIB), renowned for their high energy density and extended cycle life, are extensively utilized in electric vehicles and energy storage systems [1]. However, it poses fire risks and is prone to thermal runaway under prolonged, high-power,

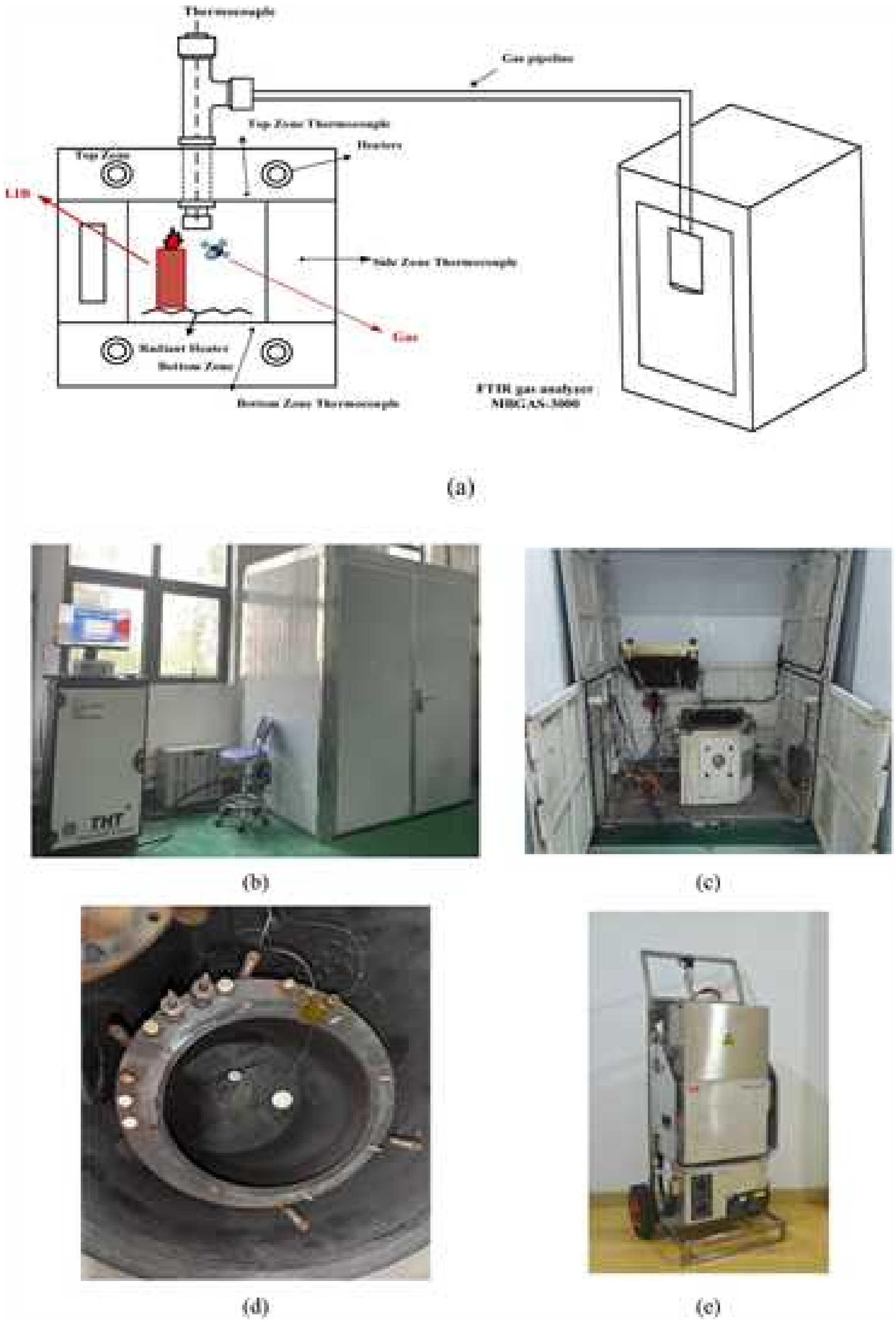

Fig. 1. The description of the experimental apparatus (a) The sketch figure of the experiment (b) The outlook of the ARC facility (c) The inner EV + Calorimeter (d) The internal configuration of ARC (e) The FTIR facility.

and abusive conditions. LIB thermal runaway is mainly categorized into overheating fire, overcharge, internal or external short circuit, and collision and puncture [2]. After the thermal runaway happens in the LIB, a significant amount of heat and combustible gases are generated, which can result in fires and explosions [3]. To reduce the fire risk, the immersion cooling technology using fluorinated agents is used in the thermal management of LIB [4]. The most widely used method is believed to be the liquid cooling immersion system [5]. Liquid cooling technology efficiently reduces fire risk regarding the LIB system in the enclosed environment because the flame is successfully prohibited in the immersion system [6]. However, the thermal runaway of LIB cannot be eliminated. Therefore, the impact mechanism of thermal runaway on liquid cooling agents in the engineered fluid immersion system must be clarified urgently.

In recent years, the thermal runaway behavior of power batteries has been widely studied. The related work mainly focuses on the critical temperature for thermal runaway [7], battery thermal behavior [8,9], thermal characteristics [10,11], the effects of ageing [12], arrangement [13], types of internal short circuits [14], positive and negative electrode materials [15], and the composition of gases during thermal runaway [16]. The charge state [17,18], the position of heating [19], and the path and likelihood of thermal runaway propagation are also investigated [20]. With the development of submerged liquid cooling technology, the thermal runaway model has also changed [21,22]. Although the submerged liquid cooling system improves temperature control, the thermal runaway of the LIB could not be stopped [23,24]. Regarding the immersion system using engineered fluid, the current research primarily centers on the design of the cooling system piping [25–27], cooling methods [28,29], type of cooling agent [30,31], loading method [32], cooling effectiveness [33], safety performance [34], corrosive gases [35], and so on. In summary, employing a submerged liquid cooling system can suppress the flame and reduce the thermal runaway effect of the battery. However, there needs to be a more comprehensive understanding of the impact of a thermal runaway on the temperature of the cooling agent. Further research is required to study the coupling mechanism between the physical parameters of the cooling agent and the temperature change.

In this study, the thermal runaway behavior of LIB is investigated by using ARC and FTIR. The maximum surface temperature and gas composition during thermal runaway are obtained, a thermal runaway model under submerged liquid cooling based on experimental data is developed, and the effects of liquid refrigerant parameters on battery thermal behavior are explored numerically. Then, the dimensionless relationships among 10 factors are proposed to describe the impact of refrigerant agent properties on its heating rate.

2. Experimental and numerical configurations

2.1. Experimental materials

The 18650 is a typical cylindrical LIB with a diameter of 18 mm, a height of 65 mm, a nominal capacity of 2600 mAh, a maximum charging voltage of 4.2 V, a cathode material of $Li\ (NiMnCo)_{1/3}O_2$, and an anode material of carbon. Before this experiment, the 18650 LIB was charged at 100 % state of charge (SOC) for 24 h. The thermal runaway characteristics of the 18650 LIB at 100 % SOC were experimentally determined to determine the temperature and gas composition of the LIB during thermal runaway. This provided the necessary measurement data for the numerical modelling of critical parameters.

2.2. Experimental devices

This study performed a thermal stability hazard assessment using an EV + ARC developed by The Dow Chemical Company in 1980 [36]. The ARC instrument manufactured by Thermal Hazard Technology was used in this study [37], as shown in Fig. 1. The FTIR is connected externally to the ARC system, as shown in Fig. 1 (a). During the experiment, the ARC provided a precisely controlled adiabatic environment to simulate the exothermic reaction when heat cannot dissipate from the interior, replicating actual battery operating conditions, see Fig. 1 (b) and 1(c). Fig. 1 (d) shows the EV + calorimeter, which has a diameter of 40 cm and a depth of 44 cm. It comprises an aluminum rim, an aluminum cover, and a base equipped with eight heaters and six thermocouples for measurement and control.

The gases generated from the thermal runaway of the battery were analyzed in the experiments using the MBGAS-3000 Fourier Transform Infrared (FTIR) Spectrometer. As shown in Fig. 1 (e), the gases that can be detected are H_2O, CO_2, CH_4, HF, HCl, and so on. The spectral resolution is $1\sim64\ cm^{-1}$. The wave number accuracy is $0.01\ cm^{-1}$, the signal-to-noise ratio is more than 20000:1, the spectral range is $0.01\ cm^{-1}$, and the signal-to-noise ratio is higher than 20000:1. The high-temperature flue gas pre-processor is controlled by PID at around 180 °C, with an operating temperature stability of 0.1 °C. The gas sampling probe and the high-temperature flue gas pre-processor contain a 1 μm particulate filtration to remove ultra-fine soot. The analyzer uses an ABB Bomem wishbone interferometer for high stability and measurement accuracy. The analyzer has a built-in oxygen filter and a high-temperature flue gas pre-processor. The detector uses a DTGS detector that does not require liquid nitrogen or semiconductor cooling. In addition, all parts in contact with the sample gas are made of corrosion-resistant 316 L stainless steel, ceramics, PFA, or Viton rubber to ensure stability and measurement accuracy. The battery sample was fixed on a stand and then placed into the ARC instrument during the experiment. The pressure sensor and FTIR probe were mounted and fixed.

The experiment was conducted by heating to initiate thermal runaway of the battery. The experimental samples were heated to 473 K at a rate of 0.5 K/min, ARC then enters the Hot Waiting Search (HWS) mode to passively monitor the self-heating behavior of the battery and record the temperature and thermal runaway gas data of the thermal runaway process in detail.

2.3. Numerical set-up

2.3.1. Numerical methods

The volume of fluid (VOF) model is a numerical fluid dynamics simulation technique used to simulate the interfacial behavior in multiphase flows. The VOF model solves the same momentum equations for various immiscible fluids in the computational domain. The volume fractions of all phases in a computational region must sum to 1. An α_i value of 0 indicates that phase i is absent from the cell, whereas an α_i value of 1 signifies that the cell is entirely occupied by phase i, as defined in Eq. (1).

$$\sum_{i=1}^{j} \alpha_i = 1 \tag{1}$$

Where j denotes the number of phases included in the simulated system and α_i is the volume fraction of the i-th phase.

Due to the existence of phase transitions in multiphase flow systems, the phase-volume transport equation for transferring the liquid phase to the gas phase can be obtained by Eq. (2) [38].

$$\frac{\partial \alpha}{\partial t} + \nabla \cdot (u\alpha) = 2\dot{m}\left(\frac{1}{\rho_{vap}} - \frac{1}{\rho_{liq}}\right)\alpha - \frac{\dot{m}}{\rho_{vap}} \tag{2}$$

Where $\frac{\partial \alpha}{\partial t}$ is the time derivative term, $\nabla \cdot (u\alpha)$ is the convection term, $2\dot{m}\left(\frac{1}{\rho_{vap}} - \frac{1}{\rho_{liq}}\right)\alpha - \frac{\dot{m}}{\rho_{vap}}$ is the phase change source term, α is the phase fraction, u is the fluid velocity, $\dot{m}$ is the evaporation mass transfer rate per unit volume, ρ_{vap} is the gas phase density, ρ_{liq} is the liquid phase density.

Within the defined simulation domain, all phases must be explicitly specified, and the volume fractions of the phases are required to satisfy Eq. (3) throughout the computational region.

$$\sum_{i=1}^{j} Y_i = 1 \tag{3}$$

The continuity equation is a specific application of the law of conservation of mass in fluid mechanics. It assumes that velocity and density are continuously differentiable functions of spatial coordinates and time [39]. The continuity equation for an incompressible fluid is shown in Eq. (4):

$$\frac{\partial \rho}{\partial t} + \nabla \cdot (\rho u) = 0 \tag{4}$$

Combining the continuity equation, considering gravity and surface tension, the incompressible momentum equation is shown in Eq. (5) [40].

$$\frac{\partial (\rho u)}{\partial t} + \nabla \cdot (\rho u u) = -\nabla p + \nabla \cdot \left[\mu\left(\nabla u + \nabla u^{T}\right)\right] + \rho g + f \tag{5}$$

Because of the energy transfer accompanying the phase transition process, it is necessary to establish and solve the energy equation. The energy equation is based on the first law of thermodynamics. In the OpenFOAM multiphase flow solver, the energy conservation equation for incompressible fluids is expressed as shown in Eq. (6) [41].

$$\rho \frac{\partial E}{\partial t} = -\rho \nabla \cdot (uE) + \nabla \cdot (\lambda \nabla E + \tau \cdot u) \pm S_h \tag{6}$$

2.3.2. Phase transition model

OpenFOAM has two different types of phase change models built inside, the Lee model and the Kinetic Gas Evaporation model, both of which are used to describe the process of phase transition between the liquid phase and the gas phase. The Lee model is based on the relationship between the mass transfer rate and the driving force of the phase transition (temperature difference or pressure difference), and the Kinetic Gas Evaporation model is based on molecular dynamics and follows the process of gas molecules hitting the liquid surface and escaping into the gas phase. The cooling agent phase change due to thermal runaway of lithium batteries in this study is mainly due to temperature difference, so the Lee phase change driving model is chosen. The control equations of this model are shown in Eq. (7) and Eq. (8) [42].

(1) Melting/evaporation process when $C > 0$

$$J_{lv} = \beta \rho \alpha \frac{|T - T_{activate}|}{T_{activate}}, T > T_{activate} \tag{7}$$

(2) Solidification/condensation process when $C < 0$

$$J_{vl} = -\beta\rho\alpha\frac{|T - T_{activate}|}{T_{activate}}, T < T_{activate} \tag{8}$$

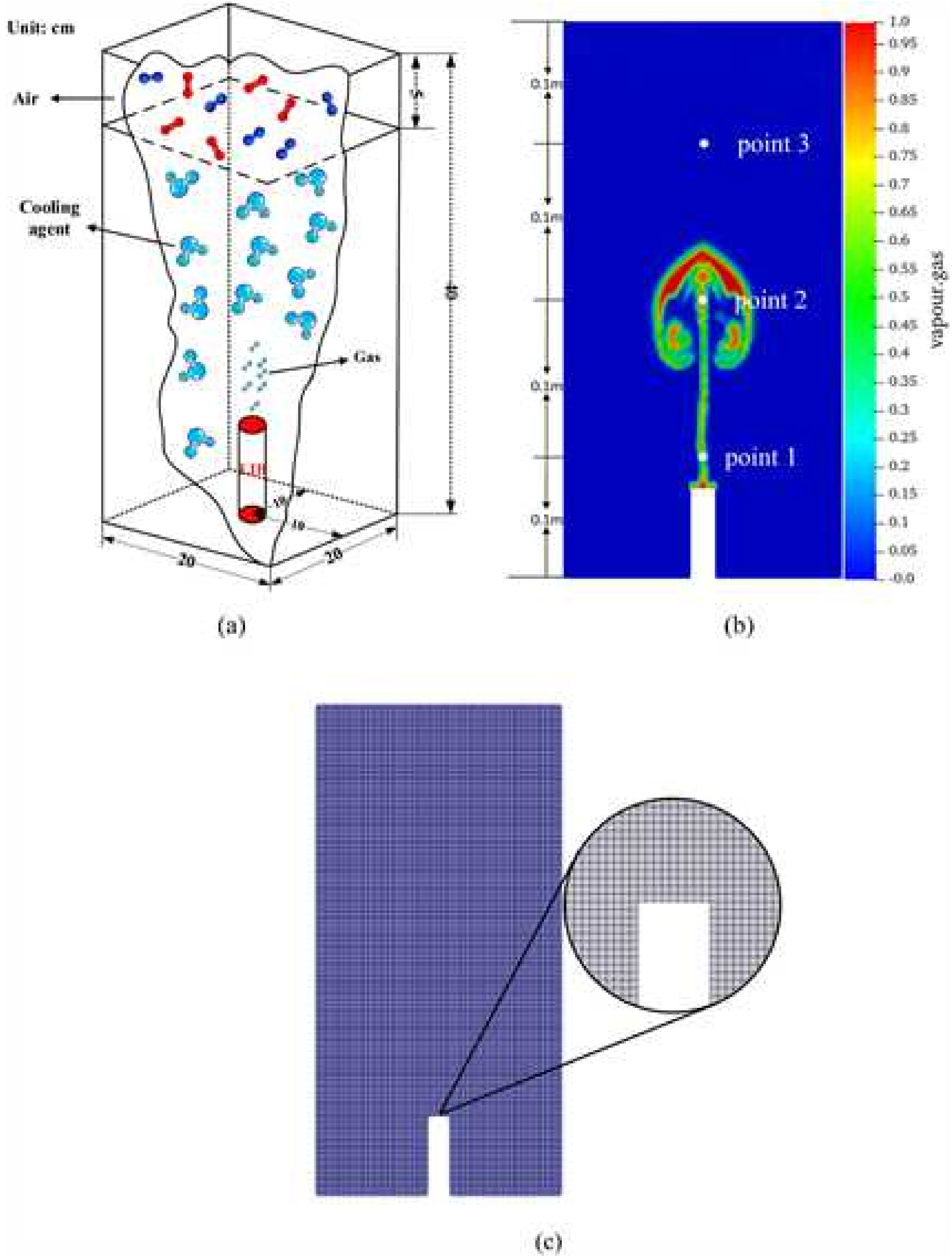

Fig. 2. The illustration of simulation configuration and computational regions (a) Configuration model (b) computational sketch figure (c) Computational mesh diagram.

in openFOAM, the total evaporation rate of the whole region is further obtained by discretely summing the evaporation rates of all control bodies, as shown in Eq. (9).

$$\dot{m} = \sum_{i=1}^{j} \mathrm{J}_{\mathrm{lv,i}} A_i \tag{9}$$

2.3.3. Turbulence model

In OpenFOAM, the traffic type used for the solution is used. This study specified the k - ε model under RAS, and the flow equations are shown in Eq. (10)–(12) [43].

Turbulent kinetic energy equation:

$$\frac{\mathrm{D}}{\mathrm{Dt}}(\rho \mathrm{k}) = \nabla \cdot (\rho \mathrm{D_k} \nabla \mathrm{k}) + \mathrm{P_k} - \rho\varepsilon \tag{10}$$

The dissipation rate equation for turbulent kinetic energy:

$$\frac{\mathrm{D}}{\mathrm{Dt}}(\rho\varepsilon) = \nabla \cdot (\rho \mathrm{D}_\varepsilon \nabla\varepsilon) + \frac{\mathrm{C_1}}{\mathrm{k}}\left(\mathrm{P_k} + \mathrm{C_3}\frac{2}{3}\mathrm{k}\nabla \cdot \mathrm{u}\right) - \mathrm{C_2}\rho\frac{\varepsilon^2}{\mathrm{k}} \tag{11}$$

Turbulent viscosity equation:

$$\mathrm{v} = \mathrm{C_V}\frac{\mathrm{k}^2}{\varepsilon} \tag{12}$$

OpenFOAM further modifies the above equations to ensure that various solvers can invoke the turbulence model. The modified turbulent kinetic energy equation and turbulent kinetic energy dissipation rate equation are shown in Eq. (13)–(18) [44].

$$\frac{\partial(\alpha\rho\varepsilon)}{\partial \mathrm{t}} + \nabla \cdot (\alpha\rho \mathrm{U}\varepsilon) - \nabla \cdot (\alpha\rho \mathrm{D}_\varepsilon \nabla\varepsilon) = \mathrm{C_1}\alpha\rho \mathrm{G}\frac{\varepsilon}{\mathrm{k}} - \left(\left(\frac{2}{3}\mathrm{C_1} - \mathrm{C_3}\right)\alpha\rho(\nabla \cdot \mathrm{U})\varepsilon - \mathrm{C_2}\alpha\rho\frac{\varepsilon}{\mathrm{k}}\varepsilon + \mathrm{S}_\varepsilon\right. \tag{13}$$

$$\frac{\partial\alpha\rho \mathrm{k}}{\partial \mathrm{t}} + \nabla \cdot (\alpha\rho \mathrm{Uk}) - \nabla \cdot (\alpha\rho \mathrm{D_k}\nabla \mathrm{k}) = \alpha\rho \mathrm{G} - \frac{2}{3}\alpha\rho(\nabla \cdot \mathrm{U})\mathrm{k} - \alpha\rho\frac{\varepsilon}{\mathrm{k}}\mathrm{k} + \mathrm{S_k} \tag{14}$$

$$\mathrm{G} = \mathrm{v_t}\left(\nabla \mathrm{U} + \nabla \mathrm{U}^{\mathrm{T}} - \frac{2}{3}(\nabla \cdot \mathrm{U})\mathrm{I}\right) : \nabla \mathrm{U} \tag{15}$$

$$\mathrm{v_t} = \mathrm{C}_\mu\frac{\mathrm{k}^2}{\varepsilon} \tag{16}$$

$$\mathrm{D_k} = \frac{\mathrm{v_t}}{\sigma_\mathrm{k}} + \mathrm{v} \tag{17}$$

$$\mathrm{D}_\varepsilon = \frac{\mathrm{v_t}}{\sigma_\varepsilon} + \mathrm{v} \tag{18}$$

In these equations, $\nabla \cdot (\alpha\rho \mathrm{D}_\varepsilon \nabla\varepsilon)$ denotes the rate of dissipation ε of turbulent diffusion (dispersion), C_μ, C_1, C_2 and C_3 are model constant.

2.3.4. Numerical configuration

To study the effect of a cooling agent on the temperature change of thermal runaway of an 18650 battery, HFE-7100 produced by 3M Company was used as the cooling agent. The boiling point, density, specific heat capacity, latent heat of vaporization, Planck's number, and surface tension are 334 K, 1520 kg/m^3, 1183 J/kg•K, 112 kJ/kg, 7.16 and 13.6 dyn/cm, respectively.

The following assumptions are made based on the physical and chemical parameters of HFE-7100. The high temperature caused by the thermal runaway of the 18650 battery only considers the upper surface of the battery. The release of the thermal runaway gas of the battery is considered, but the effect of the thermal runaway gas of the battery on the cooling agent is ignored. The simulation conceptual model is shown in Fig. 2 (a). A two-dimensional matrix computational domain with a width and height of 200 mm × 400 mm was created. Due to the weak reaction between N_2 and the cooling agent and similar thermophysical properties, to simplify the calculations and ensure accuracy, N_2 is used in this paper as an equivalent substitute for the thermal runaway released gases (mainly CO), and the gas-liquid reaction process is neglected. The computational sketch figure is shown in Fig. 2 (b). The red area represents high-temperature cooling agent vapor, while the blue area represents the cooling agent. The computational grid schematic is shown in Fig. 2 (c). The computational model is set to be at normal temperature and pressure, the initial temperature of the cooling agent is 298 K, the thermal runaway temperature on the surface of the lithium battery is 688.2 K, and the initial mass flow rate of the gas released from the thermal runaway surface is 0.0001 kg/s. The boundary conditions are set as follows: according to the simulation, the pressure at the inlet is a calculated boundary condition, the pressure is defined by the other boundary conditions and parameters, and the temperature and velocity are fixedValue. The phase volume fraction is zeroGradient boundary condition. The velocity at the outlet is the pressureInletOutletVelocity boundary, and the inletOutlet is specified as the condition when the fluid flows out, and the boundary condition details are shown in Table 1.

2.3.5. Mesh sensitivity

To accurately capture the interface while saving computational time and cost, OpenFOAM blockMesh was utilized to set up the meshes; all meshes have a mass of 1. The total number of mesh cells used for the subsequent computational analyses was determined by the mesh calculation formula Eq. (19) to be 2 mm.

$$\mathbf{D}^{*}=\left(\frac{\dot{\mathbf{Q}}}{\rho_{\infty}\mathbf{C}_{\mathbf{p}}\mathbf{T}_{\infty}\sqrt{\mathbf{g}}}\right)^{\frac{2}{5}} \tag{19}$$

At the same time, the grid sensitivity analysis is carried out, and three sizes of grids of 2.5 mm, 2.2 mm, and 2.0 mm are set up for numerical simulation. Fig. 3 shows the change of temperature with time under three different mesh sizes. It can be found that with the decrease of the mesh size, the temperature change tends to be stable, and the mesh sizes of 2.2 mm and 2.0 mm approximately overlap, and the maximum temperature difference is within 1 K. Combined with the conclusion of formula calculation and grid sensitivity analysis, the calculation grid size is determined to be 2.0 mm.

3. Results and discussion

3.1. Thermal runaway temperature distribution and flue gas content

Fig. 4 shows the temperature change with time during the thermal runaway process of the lithium battery during the experiment, and the smoke content released by the thermal runaway. At the beginning of the experiment, as the ARC continued to heat the battery, the temperature steadily increased [45]. At t = 106 min, the battery thermal runaway occurred, and the temperature instantaneously reached 688.2 K and then decreased to about 463 K in 1 s. After that, the battery temperature decreased at a rate of 0.33 K/min. When t = 470 min, the battery temperature fluctuates up and down after falling to 298 K within 6 min, as shown in Fig. 4 (a). Fig. 4 (b) shows the type and content of flue gas generated during the thermal runaway of the entire battery. CO content is the highest [16], accounting for 64 % of the total gas production; the content of HF accounts for 22 % of the total gas production, and the content of NH_3 is the lowest, which is 1 %.

3.2. Temperature distribution of cooling agent after thermal runaway

Fig. 5 shows the trend of temperature at point 3 with time without changing the physical parameters of the cooling agent. In the early stage of thermal runaway, the high-temperature area is mainly concentrated on the upper surface of the battery, and the phase change is mainly concentrated in this area. The heat begins to transfer in the whole liquid cooling system, and the cooling agent rises gently at a rate of 0.24 K/s. At t = 145 s, the temperature at point 3 reaches 341 K, the boiling point of the cooling agent. The heat dissipation capacity of this point reaches its limit, and the heat is transferred to the surrounding area. After about 5 s, the temperature in the area around point 3 reaches the boiling point as a whole, and the heat transfer slows down, resulting in a faster temperature rise to 625 K in 40 s. This time is the critical temperature rise time of the cooling agent. During t = 185 s–300 s, the temperature of the whole liquid cooling system reached the boiling point of the cooling agent, and the temperature remained stable at about 625 K.

Fig. 6 shows the cooling agent temperature variations with time. At t = 0 s, the temperature field is uniform throughout the region, and the system is at a standstill. When the t approaches 30 s, the cooling agent starts to absorb heat and spreads around. A precise temperature differentiation occurs near the thermal runaway surface, and the temperature at point 3 reaches 305.4 K. When t = 60 s, the temperature further increases to 313.86 K with an increase of 2.77 %. At the same time, the cooling agent continues to dissipate heat, allowing the heat to spread over a larger area. At t = 90 s, the temperature reaches 322.39 K with an increase of 2.71 %. When t = 120 s, the temperature of point 3 has reached 329.05 K, and the temperature of the whole region reaches more than 325 K. The cooling agent effectively transfers heat in the entire area, and the temperature of the whole system starts to become uniform. Finally, as the time approaches 150 s, the temperature of point 3 increases to 355.1 K with an increase of 7.91 %. This is caused by the temperature of the whole system reaching the boiling point of the cooling agent, and the cooling agent no longer inhibits heat diffusion.

Table 1
Setting of boundary conditions.

	inlet	outlet	wall
P	calculated	calculated	calculated
T	fixedValue	inletOutlet	zeroGradient
U	flowRateInletVelocity	pressureInletOutletVelocity	fixedValue
Alpha	zeroGradient	inletOutlet	zeroGradient

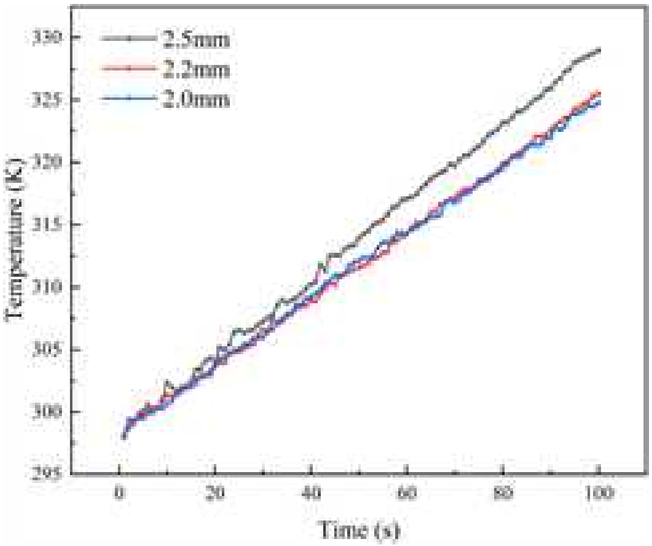

Fig. 3. Mesh sensitivity analysis.

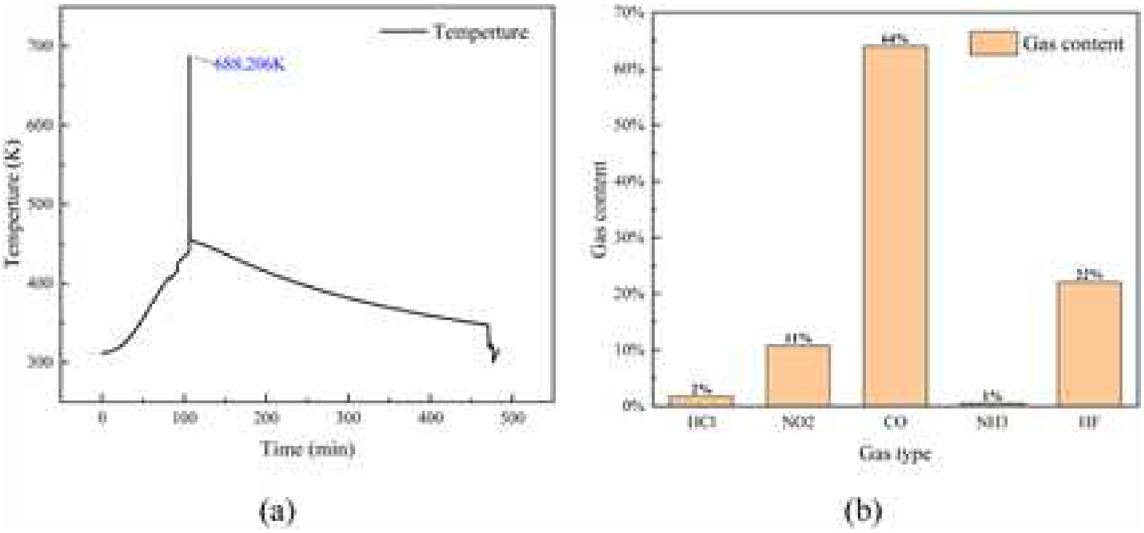

Fig. 4. The temperature distribution of the cooling agent with time (a) Temperature variation with time during thermal runaway (b) Flue gas content released by thermal runaway.

3.3. *The influence of physical parameters on the temperature rising rate*

3.3.1. *Boiling point*

The effect of boiling point (BP) on the temperature distribution is shown in Fig. 7. Under these conditions, the temperature distribution of the cooling agent shows a significant limitation at the beginning. As the boiling point increases, the temperature distribution at 30 s becomes more limited, with heat concentrated only in the nearest part of the heat source. At the same time, other regions are cooler. At 90 s, the heat is transferred over a wider area. At lower boiling points, the temperature field of the entire system reaches over 320 K, and the temperature distribution is more uniform over the entire area. At higher boiling points, the heat is concentrated near the thermal runaway surface at about 340 K. Overall, the cooling agent reaches the rapid warming stage earlier at lower BP. In general, the cooling agent reaches the rapid warming stage earlier at lower BP, and the rapid warming stage is gradually delayed with the increase of BP, and the maximum delay time reaches more than 60 s.

3.3.2. *Heat capacity*

Fig. 8 shows the effect of specific heat capacity (CP) on the temperature distribution, where the specific heat capacity of the cooling agent varies from −20 % to +20 %. The results show that the CP fluctuates above and below ±10 % and ±20 % of the baseline value,

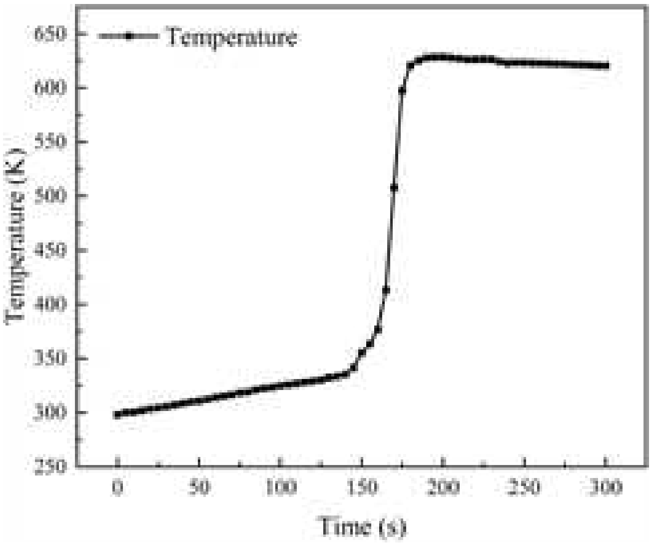

Fig. 5. Cooling agent temperature variation with time.

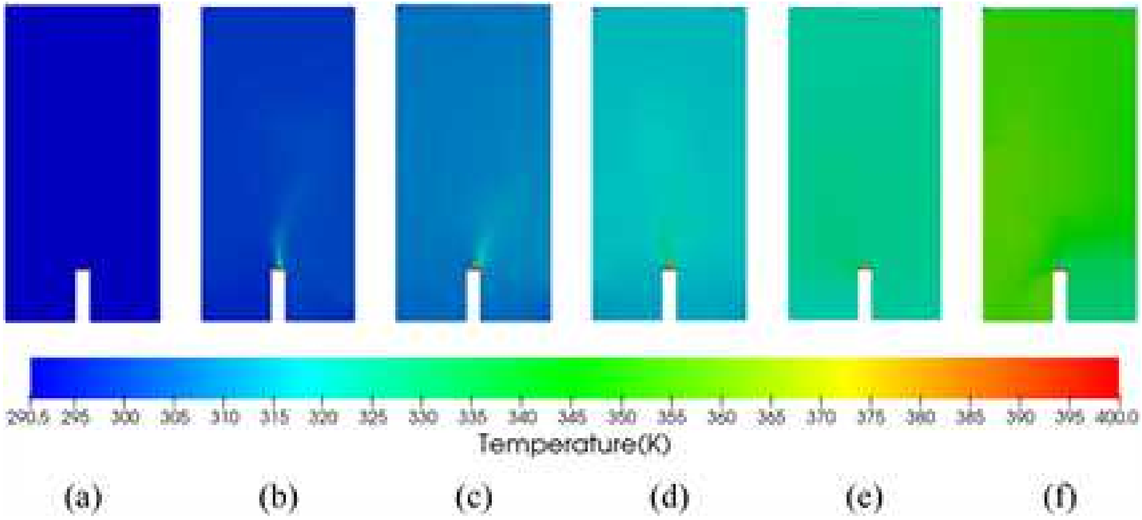

Fig. 6. The temperature distribution of cooling agent with time (a) t = 0 s (b) t = 30 s (c) t = 60 s (d) t = 90 s (e) t = 120 s(f) t = 150 s.

which significantly modulates the thermal response of the system. At t = 60 s, the cooling agent with lower CP (e.g., 946.4 and 1067.7 J/kg·K) absorbs the heat faster, resulting in a rapid increase in the temperature near the thermal runaway surface, and the high temperature region is expanded in a strip-like manner, with a wider range of thermal diffusion, while in the case of higher CP, the cooling agent has a stronger ability to absorb the heat, and the high temperature region is more concentrated, with a smoother temperature gradient. In the case of higher CP, the cooling agent absorbs heat more strongly, the high-temperature area is more concentrated, and the temperature gradient is smoother. By 120 s, the temperature increase in the low CP case reaches 9.16 % and 4.98 %, and the high temperature region is obviously expanded; while the increase in CP effectively suppresses the temperature increase, and the temperature only rises from 312.24 K to 325.16 K, and the heat is concentrated in the vicinity of the thermal runaway surface. Fig. 8 (c) further verifies this trend. Higher CP significantly delays the rapid temperature rise stage and effectively slows down the expansion of thermal runaway, while lower CP enters the rapid temperature rise process earlier, which leads to the weakening of the cooling effect. In summary, the specific heat capacity of the cooling agent is a key parameter affecting the thermal stability and cooling performance of the system.

3.4. *The influence of physical parameters on the temperature rising rate*

Fig. 9 shows the effect of different physical parameters on the time required for the cooling agent to reach the critical temperature.

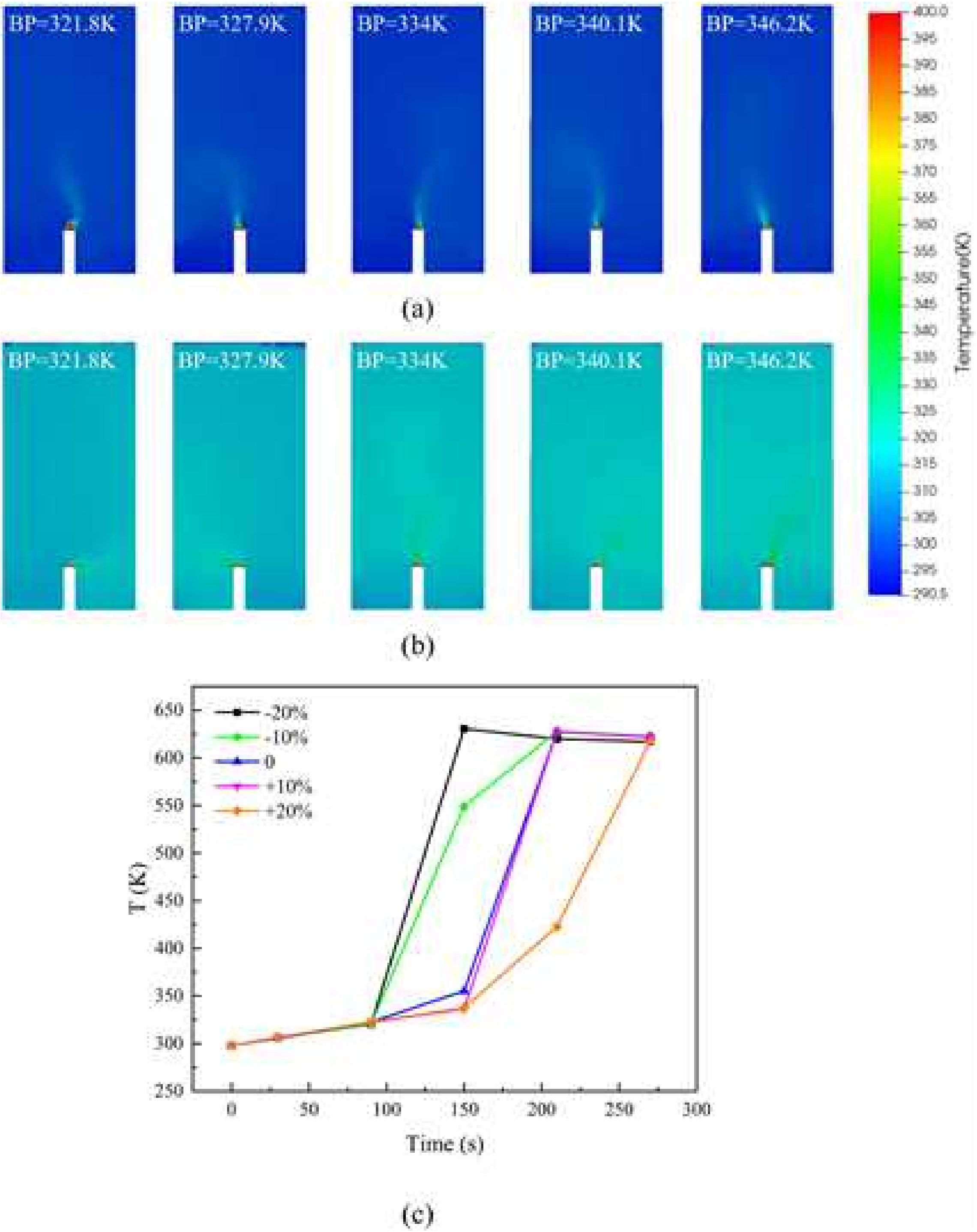

(a)

(b)

(c)

Fig. 7. The temperature change at point 3 after changing the cooling agent BP (a) when t = 30 s cooling agent temperature change (b) when t = 90 s cooling agent temperature change (c)Temperature variation curves for different BP at point 3.

BP and CP showed a significant positive correlation. As the rate of change continues to increase from −20 % to +20 %, the critical temperature rise time is delayed from 110 s to 180 s by changing BP. This indicates that the higher the boiling point, the stronger the effect of the cooling agent in retarding the temperature rise. Similarly, changing CP shows a similar trend. The higher CP, the cooling agent can absorb more heat and further retard the temperature rise. In this work, HF is the latent heat of vaporization, RHO is the density, and PR is the Prandtl Number. This indicates that these parameters have less effect on the critical temperature rise time in the

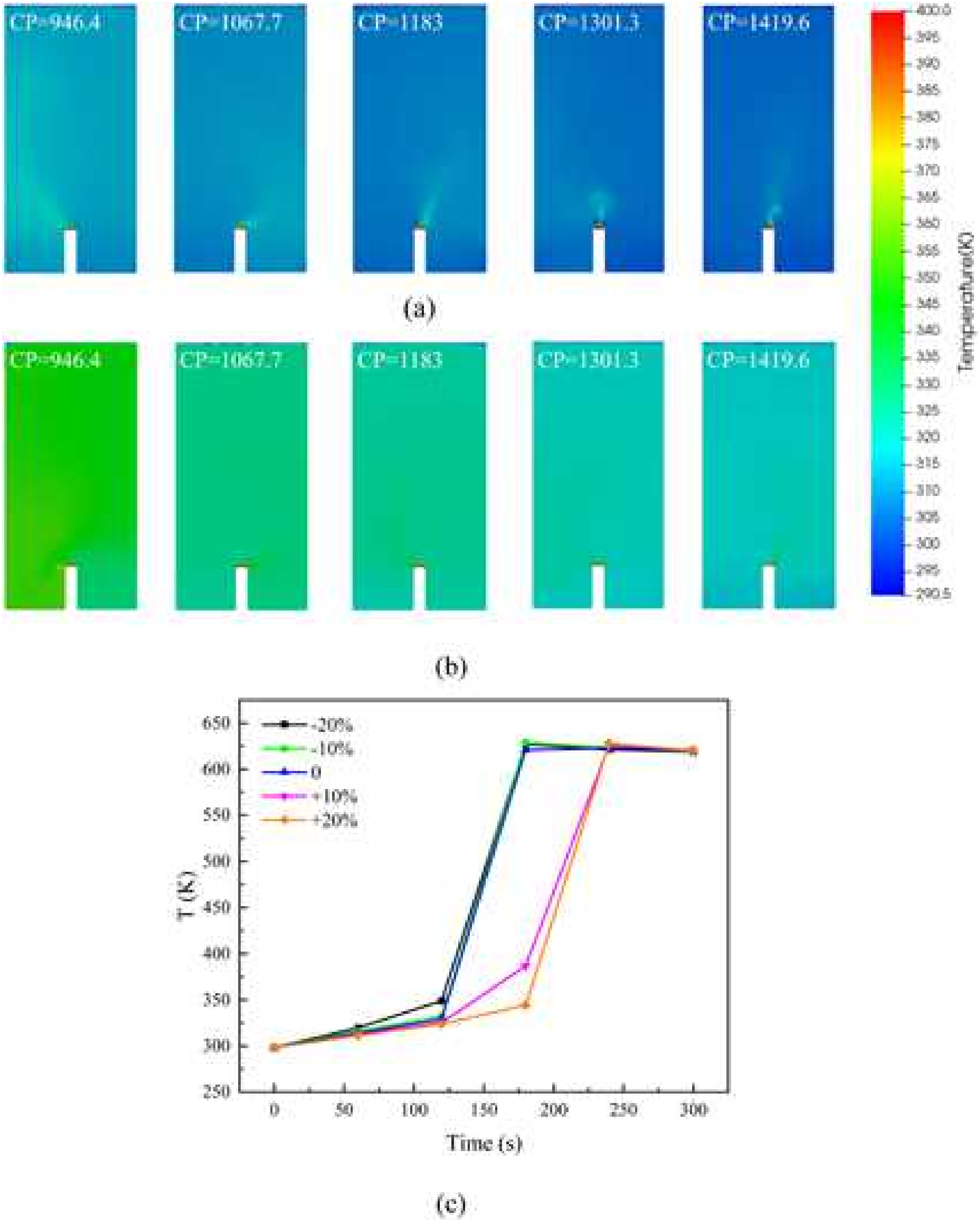

Fig. 8. The temperature change at point 3 after changing the cooling agent CP (a) t = 60 s cooling agent temperature change (b) t = 120 s cooling agent temperature change (c) Temperature variation curves for different CP at point 3.

current condition. Among them, the critical temperature rise time of HF is enhanced at −20 % and +20 %, but the overall effect is not significant. In summary, BP and CP are the main factors affecting the rise in the cooling agent temperature, while HF, RHO, and PR have relatively small effects.

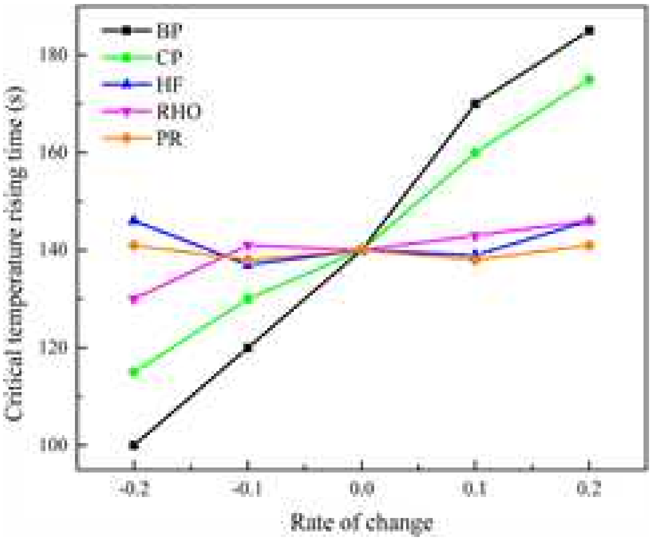

Fig. 9. The relationship between the rate of change and critical temperature rising time.

3.5. *The mechanism of physical chemistry parameters impacting on the cooling agent performance*

In the case of a battery thermal runaway, different cooling agents will affect the temperature conduction situation to various degrees. The mechanism underlying this phenomenon is interpreted in terms of the properties properties of the cooling agent. Regarding physical properties, BP, CP, etc., all directly impact a substance's heat absorption capacity. In this paper, based on the physicochemical parameters and other factors of the cooling agent, the prediction model of the temperature change of the cooling agent is established by quantitative analysis. The temperature variation $\Delta\mathbf{T}$ is related to 9 variables, as shown in Eq. (20). $\mathbf{T_0}$ is the external environmental temperature at which the submerged lithium-ion battery system operates, h is the vertical distance between the temperature acquisition point and the surface of the battery of thermal runaway. The dimensions of the above parameters are shown in Table 2. Where M, T, L, θ, and N are the dimensional expressions of mass, time, length, temperature, and the amount of substance, respectively.

$$\Delta\mathbf{T}=\mathbf{f}(\boldsymbol{\rho},\mathbf{T},\mathbf{C_V},\mathbf{H},\mathbf{F},\mathbf{Pr},\mathbf{T_0},\mathbf{h},\mathbf{t}) \tag{20}$$

M, N, L, T and θ are selected as the primary factors, F, T_0h, t are as the fundamental physical quantities, respectively. The dimensional equations of the physical remaining amounts are shown in Eq. (21):

$$\begin{cases} \pi_1 = F^{\beta_1}T_0{}^{\gamma_1}h^{\sigma_1}t^{\tau_1}H = \left[MT^{-2}\right]^{\beta_1}[\theta]^{\gamma_1}[L]^{\sigma_1}[T]^{\tau_1}\left[L^2T^{-2}\right] \\ \pi_2 = F^{\beta_2}T_0{}^{\gamma_2}h^{\sigma_2}t^{\tau_2}C_V = \left[MT^{-2}\right]^{\beta_2}[\theta]^{\gamma_2}[L]^{\sigma_2}[T]^{\tau_2}\left[L^2T^{-2}\theta^{-1}\right] \\ \pi_3 = F^{\beta_3}T_0{}^{\gamma_3}h^{\sigma_3}t^{\tau_3}pr = \left[MT^{-2}\right]^{\beta_3}[\theta]^{\gamma_3}[L]^{\sigma_3}[T]^{\tau_3}\left[M^0L^0T^0\theta^0N^0\right] \\ \pi_4 = F^{\beta_4}T_0{}^{\gamma_4}h^{\sigma_4}t^{\tau_4}T = \left[MT^{-2}\right]^{\beta_4}[\theta]^{\gamma_4}[L]^{\sigma_4}[T]^{\tau_4}[\theta] \\ \pi_5 = F^{\beta_5}T_0{}^{\gamma_5}h^{\sigma_5}t^{\tau_5}\rho = \left[MT^{-2}\right]^{\beta_5}[\theta]^{\gamma_5}[L]^{\sigma_5}[T]^{\tau_5}\left[ML^{-3}\right] \\ \pi_6 = F^{\beta_6}T_0{}^{\gamma_6}h^{\sigma_6}t^{\tau_6}\Delta T = \left[MT^{-2}\right]^{\beta_6}[\theta]^{\gamma_6}[L]^{\sigma_6}[T]^{\tau_6}[\theta] \end{cases} \tag{21}$$

Table 2
The introduction of each parameter.

Operating parameter	Notation	unit	Scalar equation
quality	m	kg	M
molar mass	m_0	g/mol	MN^{-1}
Density	ρ	kg/m^3	ML^{-3}
Boiling point	T	K	θ
constant-pressure heat capacity	C_V	J/(kg·K)	$L^2T^{-2}\theta^{-1}$
latent heat of vaporization	H	kJ/kg	L^2T^{-2}
Surface tension	F	dyne/cm	MT^{-2}
Prandtl number	Pr	1	$M^0L^0T^0\theta^0N^0$
Environmental temperature	T_0	K	θ
Temperature variation	ΔT	K	θ
Heights	h	m	L
Critical temperature rising time	t	s	T

The dimensionless quantity is obtained as shown in Eq. (22):

$$\begin{cases} \pi_1 = \dfrac{t^2}{h^2}H \\ \pi_2 = \dfrac{T_0 t^2}{h^2}C_V \\ \pi_3 = Pr \\ \pi_4 = \dfrac{T}{T_0} \\ \pi_5 = \dfrac{h^3}{Ft^2}\rho \\ \pi_6 = \dfrac{\Delta T}{T_0} \end{cases} \tag{22}$$

Eq. (22) can be simplified as Eq. (23):

$$f = \left(\frac{t^2}{h^2}H, \frac{T_0 t^2}{h^2}C_V, Pr, \frac{T}{T_0}, \frac{h^3}{Ft^2}\rho, \frac{\Delta T}{T_0}\right) = 0 \tag{23}$$

Further simplification is obtained in Eq. (24):

$$\frac{\Delta T C_V}{HPr} = f\left(\frac{Tt^2F}{T_0\ Pr^2 h^3 \rho}\right) \tag{24}$$

As we all know, $\frac{\Delta T}{t}$ is the average temperature raising rate, so let $\frac{\Delta T}{t} = k$.Eq. (24) can be simplified as Eq. (25):

$$\frac{ktC_V}{HPr} = f\left(\frac{Tt^2F}{T_0\ Pr^2 h^3 \rho}\right) \tag{25}$$

Let $\lambda = \frac{Tt^2F}{T_0\ Pr^2h^3\rho}$, $\alpha = \frac{tC_V}{HPr}$, then Eq. (26) is obtained:

$$\alpha k = A\lambda^B \tag{26}$$

Where A and B are constants. Numerical simulation was used to establish a data set of physicochemical properties of the cooling agent. The BP, CP, H, Pr, RHO, and k were statistically determined for the varying change.

Based on the database of physicochemical properties of the cooling agents from numerical simulations, the provided data were combined with the heating rate prediction model to calculate the λ value for each cooling agent. Based on the calculation results, the parameters A and B were determined using the Origin plotting software. The final prediction equation for the cooling agent heating rate in the thermal runaway of the battery inside the cooling agent was derived, as shown in Eq. (27) ($R^2 = 0.93$).

$$\alpha k = 5.68421\lambda^{0.45933} \tag{27}$$

As shown in Fig. 10, this equation can be used to predict the cooling agent average temperature rise rate after thermal runaway of a battery under immersion cooling conditions.

4. Conclusions

This paper proposes and theoretically analyzes a new method to study the mechanism of battery thermal runaway on cooling agent temperature under a liquid-cooled environment. The maximum temperature of the thermal runaway of the battery and the type of gas produced are determined through experiments. The OpenFOAM software was used for numerical simulation based on the experimental data. The influence of the physical parameters of the cooling agent on the temperature variation of the cooling agent after the battery thermal runaway in a submerged cooling environment was analyzed. The following results are obtained:

(1) In the simulation process, the thermal runaway surface appears to have a noticeable temperature difference in the initial stage. As the thermal runaway continues, the cooling agent absorbs heat, and the overall cooling agent temperature increases, but the temperature gradient decreases over time.

(2) Different physical parameters of a cooling agent have different effects on its temperature rising rate. With the change of BP and CP from −20 % to +20 %, the critical temperature rise time of the cooling agent is extended by 85 % and 52.17 %, respectively. The time to reach the necessary temperature of the cooling agent can also be changed by changing other parameters, but it is not significant compared with BP and CP.

(3) Based on the numerical simulation results, the effect of the cooling agent's physical parameters on the temperature was investigated using a dimensionless equation. This equation elucidates the relationship between the cooling agent temperature increase rate and the physical parameters after the thermal runaway of submerged cooling batteries.

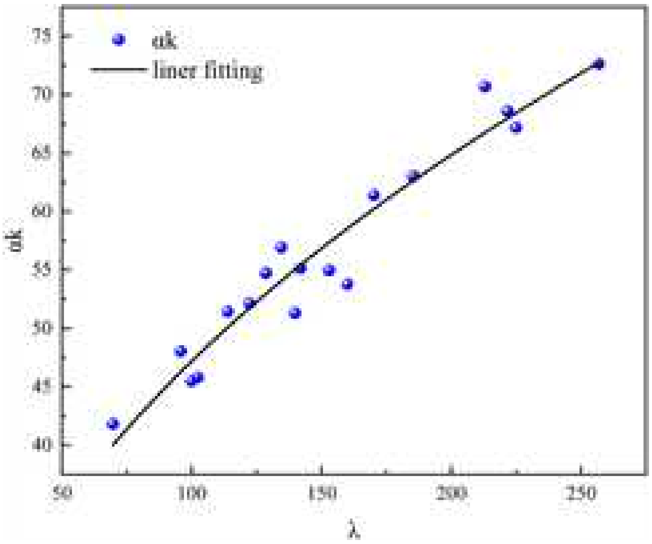

Fig. 10. The relationship of λ versus αk

The prediction model can be used to evaluate the cooling effect of the cooling agent and provide a theoretical basis for selecting the appropriate type of battery immersion cooling agent in the future. In order to further improve the accuracy and applicability of the model, future improvements will focus on capturing the entire process from the start of abnormal heating to the end of thermal runaway, combined with the simulation of the internal reaction of the battery. In addition, integrating the data of different types of batteries into the prediction model to improve the generalization of the prediction model is also one of the improvement directions. Through the exploration of the above improvement direction, a more accurate and comprehensive prediction model will be further developed.

CRediT authorship contribution statement

Biao Zhou: Supervision. **Wei Li:** Writing – original draft. **Hideki Yoshioka:** Supervision, Resources. **Kai Wang:** Project administration, Investigation. **Xukun Sun:** Visualization, Formal analysis. **Wei Wang:** Writing – review & editing. **Tao Chen:** Writing – review & editing. **Yike Guo:** Writing – original draft. **Zhenxiang Tao:** Project administration, Methodology. **Chenyang Jiang:** Writing – review & editing, Writing – original draft.

Declaration of competing interest

We declare that we have no known competing financial interests or personal relationships with other people or organizations that could have appeared to influence the work reported in this paper.

Acknowledgment

This work was supported by the Ordos key research and development program (No.YF20240026),the Beijing Nova Program (No. 202504841008), the Fundamental Research Funds for the Central Universities (No. 2025ZKPYAQ03) and Key Laboratory of Electrochemical Energy Safety Ministry ofEmergency Management(No.EES2025KF06).

Data availability

Data will be made available on request.

References

[1] L. Kong, C. Li, J. Jiang, M.G. Pecht, Li-ion battery fire hazards and safety strategies, Energies 11 (2018) 2191.
[2] C.M. Vendra, A.V. Shelke, J.E. Buston, J. Gill, D. Howard, E. Read, A. Abaza, B. Cooper, J.X. Wen, Numerical and experimental characterisation of high energy density 21700 lithium-ion battery fires, Process Saf. Environ. Prot. 160 (2022) 153–165.
[3] X. Zhang, Z. Li, L. Luo, Y. Fan, Z. Du, A review on thermal management of lithium-ion batteries for electric vehicles, Energy 238 (2022) 121652.
[4] L.F. Cabeza, A. Frazzica, M. Chàfer, D. Vérez, V. Palomba, Research trends and perspectives of thermal management of electric batteries: bibliometric analysis, J. Energy Storage 32 (2020) 101976.
[5] A.K. Thakur, R. Sathyamurthy, R. Velraj, R. Saidur, A. Pandey, Z. Ma, P. Singh, S.K. Hazra, S.W. Sharshir, R. Prabakaran, A state-of-the art review on advancing battery thermal management systems for fast-charging, Appl. Therm. Eng. 226 (2023) 120303.

[6] M. Akbarzadeh, T. Kalogiannis, J. Jaguemont, L. Jin, H. Behi, D. Karimi, H. Beheshti, J. Van Mierlo, M. Berecibar, A comparative study between air cooling and liquid cooling thermal management systems for a high-energy lithium-ion battery module, Appl. Therm. Eng. 198 (2021) 117503.
[7] H. Chen, J.E. Buston, J. Gill, D. Howard, R.C. Williams, E. Read, A. Abaza, B. Cooper, J.X. Wen, A simplified mathematical model for heating-induced thermal runaway of lithium-ion batteries, J. Electrochem. Soc. 168 (2021) 010502.
[8] L. Sheng, L. Fu, L. Su, H. Shen, Z. Zhang, Method to characterize thermal performances of an aluminum-air battery, Energy 301 (2024) 131757.
[9] L. Sheng, C. Zhang, J. Xu, X. Zhang, X. Wang, Z. Zhang, In-situ characterization approach for heat-generating performances of a pouch lithium-ion battery, Appl. Therm. Eng. 256 (2024) 124081.
[10] L. Sheng, C. Zhang, J. Xu, Q. Zhou, X. Zhang, Quantitative measurement of thermal performance of a cylindrical lithium-ion battery, Measurement 239 (2025) 115458.
[11] L. Sheng, C. Zhang, L. Wang, Q. Zhou, Z. Zhang, X. Zhang, H. Zhang, Experimental-numerical studies on thermal conductivity anisotropy of lithium-ion batteries, J. Energy Storage 103 (2024) 114139.
[12] D. Ren, H. Hsu, R. Li, X. Feng, D. Guo, X. Han, L. Lu, X. He, S. Gao, J. Hou, A comparative investigation of aging effects on thermal runaway behavior of lithium-ion batteries, eTransportation 2 (2019) 100034.
[13] Z. Wang, X. Jiang, W. Ke, W. Wang, S. Zhang, B. Zhou, Effect of lithium-ion battery diameter on thermal runaway propagation rate under one-dimensional linear arrangement, Therm. Sci. Eng. Prog. 31 (2022) 101301.
[14] D. Ren, X. Feng, L. Liu, H. Hsu, L. Lu, L. Wang, X. He, M. Ouyang, Investigating the relationship between internal short circuit and thermal runaway of lithium-ion batteries under thermal abuse condition, Energy Storage Mater. 34 (2021) 563–573.
[15] X. Feng, S. Zheng, D. Ren, X. He, L. Wang, H. Cui, X. Liu, C. Jin, F. Zhang, C. Xu, Investigating the thermal runaway mechanisms of lithium-ion batteries based on thermal analysis database, Appl. Energy 246 (2019) 53–64.
[16] L. Yuan, T. Dubaniewicz, I. Zlochower, R. Thomas, N. Rayyan, Experimental study on thermal runaway and vented gases of lithium-ion cells, Process Saf. Environ. Prot. 144 (2020) 186–192.
[17] D. Kong, G. Wang, P. Ping, J. Wen, A coupled conjugate heat transfer and CFD model for the thermal runaway evolution and jet fire of 18650 lithium-ion battery under thermal abuse, eTransportation 12 (2022) 100157.
[18] J. Kim, A. Mallarapu, D.P. Finegan, S. Santhanagopalan, Modeling cell venting and gas-phase reactions in 18650 lithium ion batteries during thermal runaway, J. Power Sources 489 (2021) 229496.
[19] K. Abhilash, A. Jadhav, V.R. Kalamkar, R.D. Jilte, Numerical study on thermal runaway in a cell and battery pack at critical heating conditions with variation in heating powers, J. Energy Storage 90 (2024) 111813.
[20] H. Zhai, H. Li, P. Ping, Z. Huang, Q. Wang, An experimental-based Domino prediction model of thermal runaway propagation in 18,650 lithium-ion battery modules, Int. J. Heat Mass Tran. 181 (2021) 122024.
[21] M. Lu, X. Zhang, J. Ji, X. Xu, Y. Zhang, Research progress on power battery cooling technology for electric vehicles, J. Energy Storage 27 (2020) 101155.
[22] M. Luo, J. Cao, N. Liu, Z. Zhang, X. Fang, Experimental and simulative investigations on a water immersion cooling system for cylindrical battery cells, Front. Energy Res. 10 (2022) 803882.
[23] C. Roe, X. Feng, G. White, R. Li, H. Wang, X. Rui, C. Li, F. Zhang, V. Null, M. Parkes, Immersion cooling for lithium-ion batteries–A review, J. Power Sources 525 (2022) 231094.
[24] Y. Ye, Y. Mao, L. Zhao, Y. Chen, M. Chen, Experimental investigation of thermal runaway behavior and propagation inhibition of lithium-ion battery by immersion cooling, Appl. Therm. Eng. 256 (2024) 124093.
[25] R. Zhao, J. Gu, J. Liu, An experimental study of heat pipe thermal management system with wet cooling method for lithium ion batteries, J. Power Sources 273 (2015) 1089–1097.
[26] E. Jiaqiang, D. Han, A. Qiu, H. Zhu, Y. Deng, J. Chen, X. Zhao, W. Zuo, H. Wang, J. Chen, Orthogonal experimental design of liquid-cooling structure on the cooling effect of a liquid-cooled battery thermal management system, Appl. Therm. Eng. 132 (2018) 508–520.
[27] D. Zhao, Z. Lei, C. An, Research on battery thermal management system based on liquid cooling plate with honeycomb-like flow channel, Appl. Therm. Eng. 218 (2023) 119324.
[28] S. Lei, T. Bojun, L. Huaiyu, Z. Chunfeng, Z. Xiaojun, Static method of liquid-immersed thermal regulation for a household energy-storing with lithium-ion batteries, Energy Build. (2025) 116325.
[29] L. Sheng, H. Zhang, L. Su, Z. Zhang, H. Zhang, K. Li, Y. Fang, W. Ye, Effect analysis on thermal profile management of a cylindrical lithium-ion battery utilizing a cellular liquid cooling jacket, Energy 220 (2021) 119725.
[30] X. Liu, Z. Zhou, W.-T. Wu, L. Wei, W. Wu, Y. Li, L. Gao, Y. Li, Y. Song, Modelling for the mitigation of lithium ion battery thermal runaway propagation by using phase change material or liquid immersion cooling, Case Stud. Therm. Eng. 52 (2023) 103749.
[31] Y. Deng, C. Feng, E. Jiaqiang, H. Zhu, J. Chen, M. Wen, H. Yin, Effects of different coolants and cooling strategies on the cooling performance of the power lithium ion battery system: a review, Appl. Therm. Eng. 142 (2018) 10–29.
[32] Y. Li, M. Bai, Z. Zhou, W.-T. Wu, J. Lv, L. Gao, H. Huang, Y. Li, Y. Li, Y. Song, Experimental investigations of liquid immersion cooling for 18650 lithium-ion battery pack under fast charging conditions, Appl. Therm. Eng. 227 (2023) 120287.
[33] Y. Ding, H. Ji, M. Wei, R. Liu, Effect of liquid cooling system structure on lithium-ion battery pack temperature fields, Int. J. Heat Mass Tran. 183 (2022) 122178.
[34] S. Wu, L. Lao, L. Wu, L. Liu, C. Lin, Q. Zhang, Effect analysis on integration efficiency and safety performance of a battery thermal management system based on direct contact liquid cooling, Appl. Therm. Eng. 201 (2022) 117788.
[35] W. Ke, K. Wang, B. Zhou, Z. Wang, W. Wang, X. Sun, B. Qiu, Y. Han, The cooling performance of halogenated alkane fire extinguishing agent and its quantitative prediction model, Therm. Sci. Eng. Prog. 26 (2021) 101093.
[36] D. Townsend, J. Tou, Thermal hazard evaluation by an accelerating rate calorimeter, Thermochim. Acta 37 (1980) 1–30.
[37] F. Liu, Q. Hu, C. Jiang, Y. Xu, P. Yan, X. Sui, The suppression performance of fluorinated cooling agents on the lithium-ion batteries fire based on the Accelerating Rate Calorimeter (ARC), Therm. Sci. Eng. Prog. 42 (2023) 101877.
[38] G. Giustini, R.I. Issa, A method for simulating interfacial mass transfer on arbitrary meshes, Phys. Fluids 33 (2021).
[39] L. Van Hoecke, D. Boeye, A. Gonzalez-Quiroga, G.S. Patience, P. Perreault, Experimental methods in chemical engineering: computational fluid dynamics/finite volume method—CFD/FVM, Can. J. Chem. Eng. 101 (2023) 545–561.
[40] Y. Xiang, D. Fang, Y. Deng, L. Zhao, W. Ma, A numerical study on melt jet breakup in a water pool using coupled VOF and level set method, Nucl. Eng. Des. 426 (2024) 113363.
[41] N. Scuro, M. Poschmann, O. Beneš, M. Piro, Progress in coupling computational thermodynamics and computational fluid dynamics to support molten salt reactor applications, Conference Paper: G4SR4 (2022) 1–15.
[42] S.C. De Schepper, G.J. Heynderickx, G.B. Marin, Modeling the evaporation of a hydrocarbon feedstock in the convection section of a steam cracker, Comput. Chem. Eng. 33 (2009) 122–132.
[43] M.M. Rahman, K. Hasan, Z. Zhu, Development of a One Equation Eddy Viscosity Model Based on k-epsilon and RAS Turbulence Models, AIAA SCITECH 2022 Forum, 2022, p. 485.
[44] D.B. Spalding, Numerical Prediction of Flow, Heat Transfer, Turbulence and Combustion, Elsevier, 2015.
[45] C.F. Lopez, J.A. Jeevarajan, P.P. Mukherjee, Experimental analysis of thermal runaway and propagation in lithium-ion battery modules, J. Electrochem. Soc. 162 (2015) A1905.